

Unraveling the Causes of the Instability of $Au_n(SR)_x$ Nanoclusters on Au(111)

Pilar Carro,* Luis Miguel Azofra, Tim Albrecht, Roberto C. Salvarezza, and Evangelina Pensa*

 Cite This: <https://doi.org/10.1021/acs.chemmater.1c00816>

 Read Online

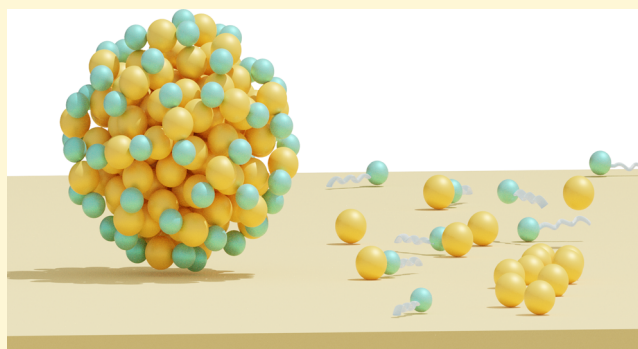
ACCESS |

 Metrics & More

 Article Recommendations

 Supporting Information

ABSTRACT: Properties of small metal nanoclusters rely on the exact arrangement of a few atoms. Minor structural changes can rapidly destabilize them, leading to disintegration. Here, we evaluate the energetic factors accounting for the stabilization and integrity of thiolate-capped gold nanoclusters (AuNCs). We found that the core-cohesive and shell-binding energies regulate the disintegration process on a solid substrate by investigating the different energetic contributions, as shown here in a combined experimental and theoretical study. As the AuNC size increases, the core-cohesive energy and shell stability (imposed by S-Au and hydrocarbon chain interactions) counterbalance the AuNC–substrate interaction and slow down the AuNC disintegration. Thus, the decomposition can not only be understood in terms of desorption and transfer of the capping molecules to the support



substrate but conversely, as a whole where ligand and core interactions play a role. Taken together, our experimental and theoretical results serve as guidelines for enhancing the stability of AuNCs on solid-state devices, a key point for reliable nanotechnological applications such as heterogeneous catalysis and sensing.

INTRODUCTION

Understanding the physicochemical contributions that control nanocluster (NC) stability in different environments is crucial for using these attractive nanomaterials in technological applications.

There have been significant advances in the synthesis, structural and physicochemical characterization of thiolate (SR)-protected gold nanoclusters (AuNCs) in the last few years. Today, the AuNC structure and stability are well described by the ‘divide and protect’ theory^{1,2} that explains the crystallographic data showing a metallic gold core protected by a shell of thiol gold complexes, $RS-(Au-SR)_x$, where x varies with the AuNC size.^{3–8}

Experimental and theoretical studies show that the shell structure plays a critical role in its stability and reactivity when AuNCs are part of colloidal systems. In fact, simple RS ligand exchange can induce changes in size or structure, for instance, the transformation of $Ag_{25}(SR)_{18}$ into $Ag_{28}(SR)_{20}$ or $Ag_{144}(SR)_{60}$ into $Ag_{133}(SR)_{52}$.⁹ Small clusters such as $Au_{25}(SR)_{18}$ in solution can associate themselves to form dimers¹⁰ or form adducts with $Ag_{25}(SR)_{18}$, resulting in NC alloys.¹¹ These reactions involve opening the RS-Au-(SR)-Au-SR shell, close sulfur–metal interactions between adjacent clusters, and place exchange of metal atoms. The latter means a reactive $Au_{25}(SR)_{18}$ NC able to interact dynamically with other thiol-covered metallic clusters.

However, the ‘divide and protect’ theory does not explain the origin of the magic size NC stability. In this case, the

superatom theory is employed.^{12–14} AuNCs are stable when their valence electrons make up a closed-shell electronic system. This theory accounts for most of the AuNC physicochemical properties but it is unable to predict the stability of AuNCs universally.¹⁵ The thermodynamic stability theory proposed by Taylor and co-workers has recently addressed this point.¹⁶ The theory predicts that the AuNC stability in colloid systems increases with the nanoparticle size, resulting in a delicate energy balance between the core-cohesive energy and the shell-to-core binding energy. Moreover, the links between the structure, stability and physicochemical properties of AuNCs are predictive.¹⁷

Despite considerable progress in understanding the stability and reactivity of AuNCs in colloid systems, relatively little attention has been paid to AuNCs on solid supports. It has been shown that Au_{20} deposited on ultrathin NaCl films undergoes sintering, which results in a highest occupied molecular orbital–lowest unoccupied molecular orbital gap reduction with increasing agglomerate size.¹⁸ Experimental studies show that the interaction of AuNCs with solid supports

Received: March 7, 2021

Revised: April 6, 2021

can destabilize the AuNCs leading, in the most extreme scenario, to the complete NC disintegration.^{19,20} Recently, it has been found that both the solid support and AuNC size have a strong influence on the heterogeneous catalysis of cyclohexane oxidation.²¹ The results show that, upon thermal air pretreatment, phenylethanethiolate-capped Au₁₄₄ clusters are more stable than their analogues Au₂₅ NCs. The higher stability was suggested to be related to the different cluster core structures, although it was pointed out that the core is stabilized by different staple motifs; Au₁₄₄ NCs exhibit only short staples (SR-Au-SR), whereas Au₂₅ NCs have long ones (SR-Au-SR-Au-SR), which may also influence the ligand removal upon pretreatment. Therefore, a key point for these nanomaterials with fascinating technological applications is to understand their behavior in contact with solid substrates.

Herein, we present an experimental and theoretical study of the stability of AuNCs on solid surfaces. Two benchmark AuNCs were chosen, Au₁₄₄(SR)₆₀ and Au₂₅(RS)₁₈ NCs. Results obtained for Au₁₄₄(SR)₆₀ placed in contact with clean reconstructed Au(111) were compared with those reported for Au₂₅(SR)₁₈ at the same NC concentration and under the same experimental conditions.^{19,22} By looking up into the different energetic contributions, we found that the traditional picture where the capping agent is the only one dictating the stability of nanoparticles does not apply in these systems. Instead, the core-cohesive energy and core–shell interactions regulate the process. These two factors counterbalance the NC–substrate interaction hence, determining the degree of AuNC disintegration on the substrate.

EXPERIMENTAL SECTION

General. The glassware employed in this work was cleaned by immersion in boiling aqueous 20% HNO₃ solution for ~30 min. Then, the material was rinsed with ultrapure water and dried in an oven at 80 °C. For AuNC synthesis, an extra cleaning step with *aqua regia* solution was carried out to remove any metal traces. All reagents and solvents were purchased from Sigma-Aldrich and were used as received (purity as stated in the text). For aqueous solutions, ultrapure water (H₂O, 18.2 MΩ·cm, Purite Select Fusion 160, UK) was employed.

Au Substrates. Two Au(111) substrates were employed. For scanning tunneling microscopy (STM) measurements, we used Au(111) single crystal disks (99.999% purity, polished with roughness <0.01 μm, and orientation accuracy <0.1°, MaTeCK GmbH, Germany). For electrochemical experiments, we employed preferentially oriented Au(111) substrates (Arrandee, Germany). Before use, the two substrates were cleaned by traditional methods, as stated in ref.¹⁹

AuNC Synthesis and Characterization. The hexanethiolate-capped Au₁₄₄ and Au₂₅ NCs were synthesized as previously reported,^{19,23,24} and a complete description of the method and characterization can be found in ref.¹⁹ In terms of unbonded thiolated species, the quality of purification was monitored by cyclic voltammetry and STM as follows. The AuNCs were dispersed in MeOH by vigorous shaking. After centrifugation (20 min and 13,400 rpm), the supernatant was collected. Then, Au(111) substrates were immersed for 24 h in the supernatant, rinsed with MeOH, and dried with N₂. Finally, the samples were studied by either cyclic voltammetry or STM. Voltammograms and STM images do not show any of the characteristic features ascribed to thiolates on Au, indicating that the unbonded-thiolates were largely removed after the purification steps were performed.¹⁹

Multiple techniques confirmed the presence of the desired AuNCs as it was previously shown in ref.¹⁹ namely, atomic force microscopy, STM, differential pulse voltammetry, and UV–vis spectroscopy. UV–

vis spectra agree with uncharged AuNCs in both cases (see Figure S1).

Sample Preparation. Au substrates were immersed in 2 μM AuNC dichloromethane (DCM) dispersion, in the dark, and at room temperature, for the lapse of time indicated in the main text. Finally, they were rinsed with DCM and dried with N₂. For in situ STM experiments in mesitylene, the Au substrates were imaged in mesitylene (98%) for about 10 min. Then, an aliquot of AuNC DCM dispersion was added to a final concentration of 3.4 μM.

Electrochemistry. Electrochemical experiments were performed with a CHI760C potentiostat (CH Instruments, United States) and a conventional three-electrode glass cell. Pt coil and a saturated calomel electrode served as the counter electrode and reference electrode, respectively. A Au substrate acted as the working electrode. Cyclic voltammograms were recorded in 0.1 M NaOH (99.99%) aqueous electrolyte at room temperature (~25 °C). The electrolyte was degassed with Ar before the measurements, while an Ar atmosphere was maintained throughout the experiments.

Scanning Tunneling Microscopy. STM measurements were performed using a Keysight 5100 STM (Keysight Technologies, United States). STM tips were prepared by mechanically cutting a Pt/Ir wire (80:20%, 0.25 mm diameter, Goodfellow, UK). All images were acquired in constant-current mode using the tunneling conditions listed in Table S1. All images are shown with line-wise flattening to remove tilt in the substrate plane and a Gaussian filter to remove the noise. STM calibration was performed for each experiment by analyzing both the HOPG surface (*x-y*) and Au steps (*z*). STM images were analyzed with WSxM software (Nanotek Electronica S.L., Spain).²⁵

Calculations Based on Density Functional Theory (DFT).

The calculations were performed using the projector augmented wave method,²⁶ as implemented in the Vienna ab initio simulation package.^{27–29} The valence electrons were described within a plane-wave basis set and an energy cutoff of 420 eV; the remaining electrons were kept frozen as core states. Electron exchange–correlation was represented by the functional of Perdew, Burke, and Ernzerhof of generalized gradient approximation.³⁰ The weak van der Waals (vdW) forces were treated by the semiempirical method of Grimme (DFT-D) where the dispersion correction term is added to the conventional Kohn–Sham DFT energy³¹ with the parameterized DFT-D3.³² The energy convergence criterion was 10^{−5} eV for self-consistent field energy except the calculation of Au₁₄₄(SR)₆₀ NCs because of the large numbers of atoms in the system (1344), the convergence process is slower than in the other calculations. The atomic positions were relaxed until the force on the unconstrained atoms was <0.031 eV Å^{−1}. The calculated Au lattice constant is 4.099 Å, which compares reasonably well with the experimental value (4.078 Å).³³ The Au₁₄₄(SR)₆₀ NC consists of a hollow icosahedral Au₁₂ kernel. The second layer is composed of 42 gold atoms exhibiting 30 triangular (111) faces. The third layer is formed by 60 gold atoms in which the polyhedron surface consists of 12 pentagons and 20 equilateral triangles. This surface is wrapped by 30 RS-Au-SR staples. For all NC structures calculated in this work, Au₁₄₄(SR)₆₀, Au₁₄₄, and Au₁₁₄, the same cubic cell used is 70 Å × 70 Å × 70 Å where the NC is separated by at least 35 Å of vacuum in all three directions. In these cases, the numerical integration was performed only in the Γ point. All atomic positions of the adsorbates, including the gold atom in the staple complex in the NC, were allowed to relax in the optimization. On the other hand, the Au(111)-(1 × 1) substrate was represented by five atomic layers and a vacuum of ~17 Å that separates two successive slabs in our calculation. Surface relaxation was allowed in the three uppermost Au layers of the slab, while the atomic coordinates of the adsorbed species were allowed to relax without further constraints. Adsorbates were placed just on one side of the slab, and all calculations include a dipole correction. An optimal grid of Monkhorst–Pack³⁴ k-points 3 × 7 × 1 was used for numerical integration in the reciprocal space of the (8 × 2√3) R30° unit cell. In the case of gas phase, the species employed an orthogonal cell of appropriate size. Spin polarization was considered in all gas-phase species.

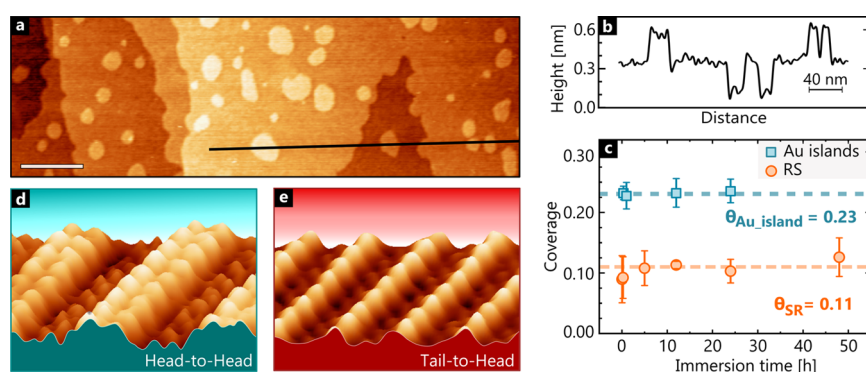


Figure 1. Characterization of the Au(111) substrate upon immersion in a Au₁₄₄(SR)₆₀ dispersion in DCM. (a) STM images showing Au islands and thiol lying-down (LD) phases on the substrate surface. The scale bar corresponds to 60 nm. (b) Height profiles along the black line in image a. The profile shows that the Au islands are monoatomic in height (0.24 nm). (c) Temporal evolution of the Au island and SR coverages. (d and e) High-resolution images of the two LD phases: head-to-head (H-H) (d) and head-to-tail (H-T) (e). The 3D images are 7 × 3 nm² in size, with a rotational angle of 180° and a tilt of 17°.

The SR and RS-Au-SR staple binding energies on Au₁₄₄(SR)₆₀ and (8 × 2√3) unit cells on the Au(111) flat surface, E_b , are defined as follows,

$$(E_b^{\text{SR}})_{\text{NC}} = \frac{1}{60} [E(\text{Au}_{144}(\text{SR})_{60})_{\text{NC}} - E(\text{Au}_{144})_{\text{NC}} - 60E(\text{SR})_{\text{gas}}] \quad (1)$$

$$(E_b^{\text{staple}})_{\text{NC}} = \frac{1}{30} [E(\text{Au}_{144}(\text{SR})_{60})_{\text{NC}} - E(\text{Au}_{144})_{\text{NC}} - 30E(\text{RS} - \text{Au} - \text{SR})_{\text{gas}}] \quad (2)$$

$$(E_b^{\text{SR}})_{\text{Au(111)}} = \frac{1}{4} [E((\text{RS} - \text{Au} - \text{SR})_2)_{\text{Au(111)}} - E(\text{Au})_{\text{Au(111)}} - 4E(\text{RS})_{\text{gas}}] \quad (3)$$

where the NC/Au(111) subscript stands for the NC/Au(111) surface, and the SR/staple superscript refers to the species for which the binding energy is calculated. A negative number indicates that adsorption is exothermic with respect to the separate clean surface and the adsorbate in the gas phase. On the other hand, the Gibbs free energy of adsorption of each surface structure (γ) can be approximated through the total energy from DFT calculations, the area (A), and the number of RS species (n) in the unit cell using eq 4:

$$\gamma = \frac{n}{A} E_b \quad (4)$$

The cohesive gold energy has been calculated as:

$$E_c = E(\text{Au}_{\text{gas}}) - E(\text{Au}_{\text{bulk}}) \quad (5)$$

where $E(\text{Au}_{\text{gas}})$ represents the energy of the Au atom in the gas phase and $E(\text{Au}_{\text{bulk}})$ represents the energy of the Au atom in the NC complete (Au₁₄₄) or without the outer shell (Au₁₁₄) as appropriate.

RESULTS AND DISCUSSION

Figure 1 shows results illustrating the decomposition of Au₁₄₄(SR)₆₀ on the Au(111) surface. STM images of the Au(111) substrate upon immersion in the NC dispersion (12 h, 2 μM in DCM) reveal Au islands, monoatomic in height (0.24 nm, Figure 1a,b) with a surface coverage $\theta_{\text{Au island}} = 0.23 \pm 0.02$ (Figure 1c), irrespective of the immersion time.

The SR moieties arrange into two types of domains, as shown in Figure 1d,e. One domain corresponds to thiolated species organized into a well-ordered phase of paired-rows separated by 2.3 ± 0.1 nm. The distance between rows is 0.57 ± 0.04 nm, and the bright spots forming each row are placed at 0.52 ± 0.01 nm (Figure 1d). This domain agrees with the

head-to-head (H-H) lying down (LD) phase reported previously.^{35–37} The second domain comprises rows of single bright spots separated by 1.26 ± 0.02 and 0.51 ± 0.01 nm (Figure 1e). This phase agrees with the head-to-tail (H-T) LD phase.^{35,38,39}

On the other hand, the total number of thiol species determined by the charge of the thiolate-Au electroreduction peak (q_{SR}) results in a thiol coverage $\theta_{\text{SR}} = 0.11 \pm 0.01$ (Figure 1c), also irrespective of the immersion time. The θ_{SR} value and its time evolution (Figure 1c) suggest that thiolated species are close-packed parallel to the Au(111) surface, reaching saturation in a relatively short time of immersion.

Before we move onto the system's energetic aspects, we will comment on the lack of vacancy islands (pits, Figure 1a). These features are fingerprints of alkanethiolate monolayers at high coverage ($\theta_{\text{SR}} = 1/3 \approx 0.33$).⁴⁰ At that coverage, molecules arrange in a dense standing-up (SU) phase as part of RS-Au-SR moieties on the Au(111) substrate. Au vacancies are proposed to emerge by removing the Au adatoms needed to form the RS-Au-SR motif. By contrast, LD phases of hexanethiolate on Au(111) usually do not show Au vacancy islands.⁴¹ RS-Au-SR moieties can nevertheless still form, based on Au adatoms supplied through the lifting of the herringbone reconstruction, which provides a significant part of the required adatoms (0.043 out of 0.063).⁴²

For the LD phases observed here, two facts suggest the RS-Au-SR moieties' presence at the interface: first, the absence of the herringbone reconstruction that is present before immersion in the NC dispersion (Figure S2), and second, the fact that the NC decomposition itself provides large amounts of Au adatoms. Indeed, by considering the experimental parameter θ_{SR} , we estimate that the expected Au island coverage would be 0.31 if AuNCs break apart into Au islands + SR and 0.25 if AuNCs break apart into Au islands + RS-Au-SR (cf. Supporting Information for further details). Comparison between experimental ($\theta_{\text{Au island}} = 0.23$) and predicted values for the Au island coverage suggests that the LD structures contain adatoms as a RS-Au-SR staple complex.

Thermodynamics of the Thiol Species on Au₁₄₄(SR)₆₀ and Au(111). To better understand the decomposition process of the Au₁₄₄(SR)₆₀ NC, the electronic and geometric structures of the thiol species on the Au₁₄₄(SR)₆₀ and the Au(111) substrate have been investigated by DFT calculations.

Our experimental data indicate that the AuNCs protected by RS-Au-SR units decompose into Au islands and LD phases containing RS-Au-SR moieties upon interaction with the Au surface. We have recently shown that the most stable configurations for H-T and H-H phases are described, in both cases, by a $(8 \times 2\sqrt{3})_{\text{rect}}$ unit cell.⁴³ The optimized structures are shown in Figure 2a,b, respectively.

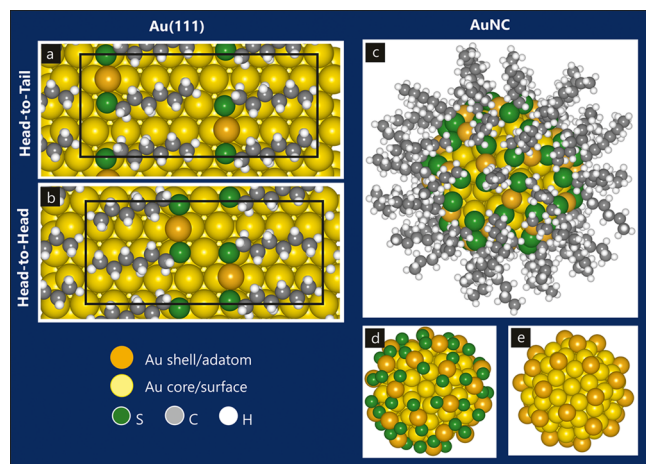


Figure 2. (a and b) Optimized structures for different LD domains on Au(111): (a) RS-Au-SR in H-T and (b) RS-Au-SR on H-H. (c) $\text{Au}_{144}(\text{SR})_{60}$ NC structure, (d) $\text{Au}_{144}(\text{SR})_{60}$ NC without the alkyl chain, and (e) Au_{144} clean structure.

Table 1 shows the SR binding energy (E_b) and the surface free energy (γ) values obtained after the optimization of each

Table 1. SR Binding Energy (E_b) and Surface Free Energy (γ) for the Different Surface Structures

LD phase	structures	unit cell	θ_{RS}	E_b/RS [eV]	γ [$\text{meV}\text{\AA}^{-2}$]
H-T	[RS-Au-SR]@Au(111)	$(8 \times 2\sqrt{3})_{\text{rect}}$	1/8	-3.73	-64.08
H-H	[RS-Au-SR]@Au(111)	$(8 \times 2\sqrt{3})_{\text{rect}}$	1/8	-3.68	-63.22
	$[\text{Au}_{144}(\text{SR})_{60}]_{\text{NC}}$	$(70 \times 70 \times 70)$	1	-2.85	-192.85

surface structure (Figure 2). The E_b values of both LD models on the Au(111) surface are higher than that for the NC because of the optimization of the alkyl chain–alkyl chain and alkyl chain–substrate interactions.

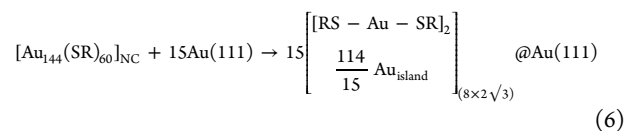
However, the thermodynamic stability is given by γ , as E_b is only an indication of how strong alkanethiolate species bond to the Au surface. Considering γ in the analysis, the SR radical on $\text{Au}_{144}(\text{SR})_{60}$ is much more stable, by a factor of 3 compared to SR in LD lattices (Table 1). The highest stability of the SR species on the AuNC, despite its lower E_b , results from the more significant molecular density, and correspondingly, more considerable coverage ($\theta_{\text{SR}} = 1$) on the cluster than on the Au(111) surface (n/A term in eq 4). Thus, as with $\text{Au}_{25}(\text{SR})_{18}$,²² the thermodynamic stability of the gold-adatom complexes by itself cannot explain the decomposition of the $\text{Au}_{144}(\text{SR})_{60}$ NC.

Thermodynamics of the Degradation Process: Small Versus Large NCs. $\text{Au}_{144}(\text{SR})_{60}$ and $\text{Au}_{25}(\text{SR})_{18}$ degradation processes lead to the same products. The decomposition

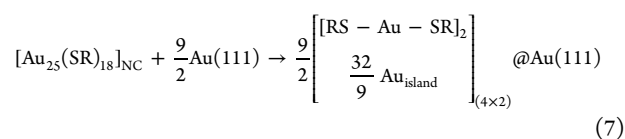
process results in Au islands and SR adsorbed on Au(111) as part of RS-Au-SR interfacial units for both NCs.

Despite the similarity, an intriguing observation is the different decomposition degrees observed between $\text{Au}_{25}(\text{SR})_{18}$ and $\text{Au}_{144}(\text{SR})_{60}$ NCs. Upon decomposition, $\text{Au}_{25}(\text{SR})_{18}$ leads to a SU lattice ($\theta_{\text{SR}} = 1/3$). In contrast, for the same experimental conditions, $\text{Au}_{144}(\text{SR})_{60}$ only leads to a LD lattice ($\theta_{\text{SR}} = 1/8$) – note that this is the case even for extended immersion times (Figure 1c). The latter reflects that the number of decomposed $\text{Au}_{144}(\text{SR})_{60}$ is lower than that of $\text{Au}_{25}(\text{SR})_{18}$. Our estimation, based on the experimental θ_{SR} values, indicates that the number of decomposed $\text{Au}_{144}(\text{SR})_{60}$ is eight times lower than that of $\text{Au}_{25}(\text{SR})_{18}$ (cf. Supporting Information). This is unexpected considering that the initial AuNC number concentration is the same for both AuNCs, and more importantly, enough to fully saturate the Au(111) surface with the SR adopting the highest packing, that is, molecules arranged in a $c(4 \times 2)$ lattice where SR adopts a SU configuration. Thus, it would be expected that both AuNCs decompose to the same degree.

Therefore, we evaluate the energetics of the complete decomposition process of the large single $\text{Au}_{144}(\text{SR})_{60}$ NC to form both H-T or H-H hexanethiolate LD phases according to reaction 6 and compare the result with that one obtained for the $\text{Au}_{25}(\text{SR})_{18}$ NC (eq 7).²²



$$(\Delta E)_{\text{H-T}} = -68.5 \text{ eV} \text{ and } (\Delta E)_{\text{H-H}} = -65.8 \text{ eV}$$



$$(\Delta E) = -21.9 \text{ eV}$$

The ΔE values show that the NC decomposition process is largely favored for a $\text{Au}_{144}(\text{SR})_{60}$ than for a $\text{Au}_{25}(\text{SR})_{18}$ NC, irrespective of the LD lattice. In fact, by setting sight on the products, the $\text{Au}_{144}(\text{SR})_{60}$ decomposition process would be favored because of two factors. First, the stabilization provided by the Au island formation is higher for $\text{Au}_{144}(\text{SR})_{60}$ than for $\text{Au}_{25}(\text{SR})_{18}$, as the former has a more available number of Au atoms per unit cell, 114 versus 16. Second, the E_b value of SR species in the surface lattice is slightly higher for LD than for the SU configuration²² (≈ -3.7 vs -3.5 eV, see Table 1).

The above argument is strictly valid at the zero-temperature limit. However, considering temperature through the entropic arguments would also favor the decomposition of the bigger AuNC. From the alkanethiolate point of view, the entropy change should be very little because their movement limitations for acquiring different conformations do not differ much between being adsorbed on a NC or a flat surface such as Au(111). Instead, the process by which the core Au atoms are released from it to be part of Au islands adsorbed on the Au(111) surface implies an increase in the freedom degrees and thus an increase in entropy. This increase would be higher for Au_{144} than Au_{25} NCs because of the higher number of core atoms.⁴⁴ Therefore, if entropy is considered in the energetic

analysis, the conclusion would not change from that at $T = 0$ K.

To sum up, eqs 6 and 7 indicate that the AuNC decomposition is favored for a $\text{Au}_{144}(\text{SR})_{60}$ than for a $\text{Au}_{25}(\text{SR})_{18}$. This conclusion contrasts the experimental data and points out that other factors should be considered in the stability analysis.

It is worth noting that reactions 6 and 7 only consider the initial and final states. In this sense, by looking into the difference within the AuNCs, we consider two potential factors that can hinder their decomposition: The Au cohesive energy and the outer shell composition.

The Au cohesive energy of the NCs is +3.00 eV for Au_{144} and +2.43 eV for Au_{25} . If we consider the Au cohesive energy of these NCs without the Au external shell, the results hardly change for Au_{144} , +2.97 eV. In contrast, for the smallest NC, the Au_{13} cohesive energy drops considerably, +2.02 eV (eq 5). In this sense, it is important to remember that the Au_{25} NC has only one outer layer around the inner Au_{13} kernel^{3,8} while the Au_{144} NC is made up of a Au_{12} kernel surrounded by three layers of 42, 60, and 30 Au atoms, respectively.^{45,46}

The second factor to be considered is the outer shell composition. For $\text{Au}_{144}(\text{SR})_{60}$ NC, the shell is formed by 30 RS-Au-RS staple motifs that account for a total stabilization energy of -105.3 eV (each of the 30 complexes contributes with -3.51 eV, Table 2). In the case of $\text{Au}_{25}(\text{SR})_{18}$, the

Table 2. Binding Energy (E_b) and vdW Energy (E_{vdW}) for the RS-Au-(SR)-Au-SR and SR-Au-SR Complexes on AuNC's Core

species	E_b [eV]	E_{vdW} [eV] ^a
[RS-Au-SR]@ Au_{144}	-3.51	-1.47 (42%)
[RS-Au-(SR)-Au-SR]@ Au_{13}	-5.18 ²²	-1.88 (36%)

^aValues in parentheses correspond to the contribution of E_{vdW} to the E_b .

stabilization energy imparted by the shell only accounts for -31.08 eV as the outer shell has only six RS-Au-(SR)-Au-SR staples (each of the six complexes contributes with -5.18 eV, Table 2). We also found that vdW energy increases with the cluster size and the number of staples in the shell. Table 2 shows that they contribute in 42% and 36% to the shell stability for $\text{Au}_{144}(\text{SR})_{60}$ and $\text{Au}_{25}(\text{SR})_{18}$, respectively. Taken together, the shell composition also points out that the $\text{Au}_{144}(\text{SR})_{60}$ presents a much higher shell-to-core interaction energy than the $\text{Au}_{25}(\text{SR})_{18}$.

After this analysis, one can conclude that the larger cluster's improved stability on the Au(111) substrate results from both higher cohesive and shell-to-core interaction energies. These energetic contributions hinder to some extent the $\text{Au}_{144}(\text{SR})_{60}$ decomposition process on the Au surface. Next, we will present experimental evidence that supports this conclusion by in situ imaging of the adsorption/decomposition process on the Au substrate.

Adsorption and Decomposition of $\text{Au}_{144}(\text{SR})_{60}$ and $\text{Au}_{25}(\text{SR})_{18}$ on the Au(111) Surface. In principle, for two particles capped with the same alkanethiol thiol, one would expect that larger particles adsorb preferably *via* vdW interactions because they have more contact sites with the surface.⁴⁷ Thus, the lower number of $\text{Au}_{144}(\text{SR})_{60}$ adsorbed and decomposed on the Au substrate cannot be explained by a difference in contact sites between the NCs and substrate

surface. One could argue that the differences in size could affect either mobility in the DCM solution or introduce steric effects during adsorption and decomposition favoring the smaller NC. The number of $\text{Au}_{144}(\text{RS})_{60}$ that reached the surface is only 2.4 higher than $\text{Au}_{25}(\text{RS})_{18}$ if diffusion is considering and even lower (1.5) if the steric effect regulates the AuNC adsorption (cf. Supporting Information). Hence, none of these effects explains the experimental results.

A detailed analysis of the STM images in Figure 3 provides evidence of the adsorption/decomposition processes' factors.

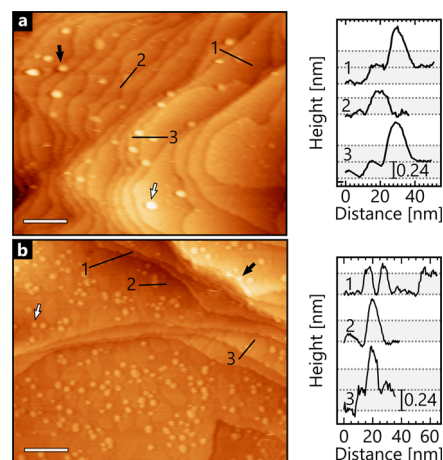


Figure 3. In situ STM images recorded in mesitylene upon addition of (a) $\text{Au}_{144}(\text{SR})_{60}$ and (b) $\text{Au}_{25}(\text{SR})_{18}$. The images show that for the big NC the degradation products are preferentially located at the steps (black arrows), while those for $\text{Au}_{25}(\text{SR})_{18}$ on the terraces (white arrows). Height profiles are included in the left panels to highlight that bright spots correspond to degradation products rather than AuNCs. The dotted lines and the shadow areas within them indicate the step height in Au(111). Scale bars correspond to 60 nm.

While the Au products originated from adsorption/decomposition of $\text{Au}_{144}(\text{SR})_{60}$ NCs are preferentially present at step edges (Figure 3a), those formed by the disintegration of $\text{Au}_{25}(\text{SR})_{18}$ NCs are randomly distributed on the Au(111) substrate (Figure 3b). It means that the $\text{Au}_{144}(\text{SR})_{60}$ shell, formed by RS-Au-SR moieties, only interacts upon contact with low-coordinated sites (more reactive) of the Au surface. On the other hand, the shell of the smaller $\text{Au}_{25}(\text{SR})_{18}$ NC formed by RS-Au-(SR)-Au-SR can also interact with the defective-free terrace (less reactive), as shown in Figure 3b. The reactivity of these small clusters is not surprising as they can form either $\text{Au}_{25}(\text{SR})_{18}$ dimers¹⁰ or adducts with $\text{Ag}_{25}(\text{SR})_{18}$ resulting in NC alloys.¹¹ These transformations involve the RS-Au-(SR)-Au-SR shell's spontaneous opening, close S-metal interactions between adjacent clusters, and place exchange of metal atoms. This means that a reactive $\text{Au}_{25}(\text{SR})_{18}$ NC is able to interact dynamically with thiol-covered metal surfaces. This conclusion agrees with simulations about the dynamics of the core-shell bonds in Au_{25} clusters that suggest a shell loosely bound to the core.⁴⁸

On the other hand, it has been shown that NC reactivity decreases with the cluster size.²¹ In this sense, a recent study on the chiral inversion of thiolated-protected gold NCs shows that the racemization mechanism and stability strongly depend on the size, core structure, and details of the metal-ligand structure.⁴⁹ Thus, a more rigid and less reactive $\text{Au}_{144}(\text{SR})_{60}$ NC is expected.

At this stage, some discussion about the solvent's role in opening the NC shell is needed. While gold island formation is a clearly surface-assisted process involving Au adatom surface diffusion, the formation of the alkanethiol phases could involve transferring SR species to the solvent and readsorption on the substrate surface. In this regard, it has been found that solvent-capping interaction can influence the ligand conformation⁵⁰ or be even stronger enough to break the Au–S bonds.⁵¹ It has been shown that dodecanethiolate-capped gold nanoparticles of 3–4 nm in size lost their ligand-molecules from the nanoparticle faces when immersed in tetrahydrofuran (THF). This process involves a selective rupture of the Au–S bond induced by the solvent environment because this process is not observed in ethanolic solutions. In our case, we can discard the solvent-assisted desorption in solution, even though THF and DCM have similar polarities. In fact, at the same NC concentration, Au₁₄₄(SR)₆₀ should leave more thiolate species to the solution than the Au₂₅(SR)₁₈. Therefore, the larger NC should also produce dense SU phases rather than the diluted LD experimentally observed (Figure 1).

This observation confirms that NC decomposition occurs at the metal substrate surface as reported for AuNCs on polycrystalline Ag²⁰ and Au(111).¹⁹ It can be argued, however, that the solvent would also play a key role in favoring the 'opening' of the RS-Au-SR or RS-Au-(SR)-Au-SR shell at the surface rather than breaking it in solution and, in this way, favoring transfer of Au-SR from the NC to the substrate. However, the effect of different solvents (ethanol, THF, and DCM) on the Au-S stretching vibration frequency in a Au-SR complex as shown by DFT calculations (not shown here) has no differences concerning the value in the gas phase. In fact, it has been reported that the thermodynamic stability of AuNCs is not affected by the solvents.¹⁶ Therefore, the S-Au breaking is a surface-assisted process where the NC shell's stability plays a key role and determines the number of thiolated species transferred from the NC to the Au(111) surface.

Mechanism of NC Decomposition on Au(111). Based on the above observations, we propose the decomposition mechanism sketched in Figure 4. After adsorption on the Au(111) substrate, the NC shell is opened by interaction with Au surface atoms from the (111) substrate (Figure 4a).

For the Au₁₄₄(SR)₆₀, the 'opening' process occurs preferentially at step edges where the RS-Au-SR moieties can break into Au-SR and SR radicals that interact with the low-coordinated Au atoms (Figure 4a,b). In fact, recent in situ imaging of thiols adsorbed on Au(111) has shown that while RS-Au-SR moieties are present at terraces, SR radicals are present at step edges.⁵² The RS-Au-SR opening by AuNC interaction with the step edge leads to the NC shell's weakness and exposes the Au core atoms to the environment. Thus, AuNCs' components start to disintegrate, leading first to the Au-SR⁵³ and Au adatoms on the surface (Figure 4b), and finally, to RS-Au-SR staples and Au islands. The fact that this process is restricted to the NC-step edge interaction besides with the high cohesive energy of this cluster results in a low population of RS-Au-SR, which accordingly accommodate in LD phases ($\theta_{\text{SR}} = 1/8$) and a relatively small number of Au islands (Figure 4c).

In contrast, for Au₂₅(SR)₁₈ NC, the opening of the RS-Au-(SR)-Au-SR shell takes place after interaction with any Au surface atom because of the high reactivity and dynamics of the shell following the mechanism already proposed in refs.^{20,22} (Figure 4d). Also, the adsorption and decomposition are

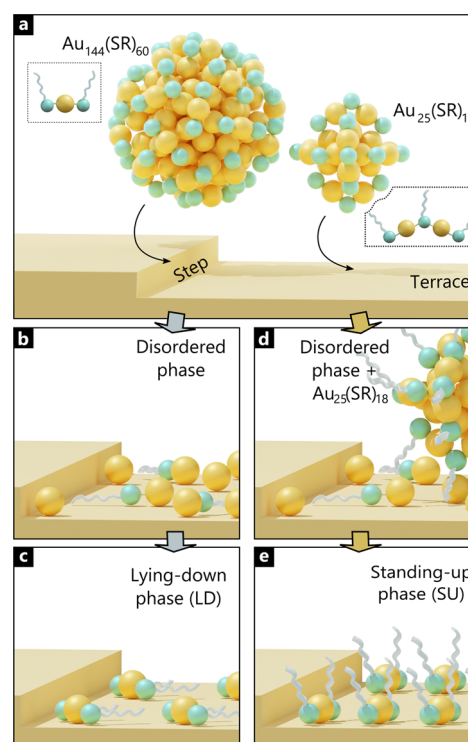


Figure 4. Sketch of the proposed decomposition process for Au₁₄₄(SR)₆₀ (left panels) and Au₂₅(SR)₁₈ (right panels). (a) Picture highlights the preferential adsorption site on the substrate: steps for Au₁₄₄(SR)₆₀ and terraces for Au₂₅(SR)₁₈. The insets show the structure of the staples forming the ligand shell. Panels b and d illustrate the formation of a disordered phase resulting upon breaking of AuNCs apart into their constituent units. As stated in panel d, Au₂₅(SR)₁₈ adsorption is enhanced by the interaction between RS-Au-(SR)-Au-SR and the moieties already present at the substrate. (c–e) Thiolated monolayers obtained as a final product of the decomposition process: LD for Au₁₄₄(SR)₆₀ (c) and SU for Au₂₅(SR)₁₈ (e). For clarity, the Au islands are not included. Yellow: Au adatoms and light green: thiol radicals.

enhanced by the interaction between RS-Au-(SR)-Au-SR and the moieties already present at the substrate (Au-SR or Au adatoms, Figure 4d). Later, the remaining AuNC's components easily disaggregate because of the low cohesion energy of the AuNC core and its interaction with the substrate surface. The surface reaction proceeds until the moieties present on the surface fully cover the surface and become unavailable for AuNC-surface dimerization; that is, because of the high SR surface concentration, the thiolates adopt the SU configuration and become unavailable to be part of the 'bridge' complexes between surface-AuNCs. This step is the formation of the SU phase ($\theta_{\text{SR}} = 1/3$) (Figure 4e).

CONCLUSIONS

We have discussed the stability of thiolated AuNCs on solids supports based on the degree of AuNC disintegration. We show experimental and theoretical results about the decomposition of Au₁₄₄(SR)₆₀ NCs on clean reconstructed Au(111) surfaces and compare them to those reported for Au₂₅(SR)₁₈ under the same experimental conditions.

Considering individual particles, the Au₁₄₄(SR)₆₀ decomposition is thermodynamically favored concerning the Au₂₅(SR)₁₈. However, its higher cohesive energy and shell stability hamper the NC disintegration to some extent.

Therefore, Au₁₄₄(SR)₆₀ disintegration takes place preferentially at the high reactive site of the substrates where the stable shell can be opened, exemplified here with low-coordinated atoms of step edges. In contrast, Au₂₅(SR)₁₈ disintegration occurs over the entire substrate surface, confirming the flexibility and reactivity of the shell and the more straightforward core decomposition. Interestingly, our results suggest that the decomposition cannot be understood in terms of the desorption of individual thiol-gold adatom complexes because the RS-Au-(SR)-Au-SR dimeric staple has larger E_b than the RS-Au-SR monomeric staple on their corresponding clusters but in terms of the rupture of the shell as a whole, where vdW forces play a significant role. Our experimental and DFT results confirm theoretical predictions about the ligand shell's increased stability with the increase in the NC size proposed for colloid systems and the extent of its validity to solid supports.

Taken together, our results point out that the AuNC reactivity can be understood from the structure of the Au-SR complexes in the shell, but the AuNC stability requires considering the AuNC as a whole, where core and shell interactions play an essential role.

■ ASSOCIATED CONTENT

SI Supporting Information

The Supporting Information is available free of charge at <https://pubs.acs.org/doi/10.1021/acs.chemmater.1c00816>.

Additional STM images, imaging acquisition parameters for STM images, determination of the RS coverage from electrochemical data and additional calculations (PDF)

■ AUTHOR INFORMATION

Corresponding Authors

Pilar Carro – Área de Química Física, Departamento de Química Facultad de Ciencias Instituto de Materiales y Nanotecnología Avda, Universidad de La Laguna, La Laguna, Tenerife 38200, Spain; orcid.org/0000-0001-8073-9857; Email: pcarro@ull.edu.es

Evangelina Pensa – Department of Chemistry, Imperial College London Exhibition, London SW7 2AZ, U.K.; orcid.org/0000-0003-1090-0830; Email: e.pensa@tum.de

Authors

Luis Miguel Azofra – Instituto de Estudios Ambientales y Recursos Naturales (i-UNAT), Universidad de Las Palmas de Gran Canaria (ULPGC), Las Palmas de Gran Canaria 35017, Spain; orcid.org/0000-0003-4974-1670

Tim Albrecht – Department of Chemistry, Imperial College London Exhibition, London SW7 2AZ, U.K.; orcid.org/0000-0001-6085-3206

Roberto C. Salvarezza – Instituto de Investigaciones Físicoquímicas Teóricas y Aplicadas (INIFTA), Facultad de Ciencias Exactas Universidad Nacional de La Plata, CONICET, La Plata 1900, Argentina

Complete contact information is available at: <https://pubs.acs.org/doi/10.1021/acs.chemmater.1c00816>

Author Contributions

The manuscript was written through contributions of all authors. All authors have given approval to the final version of the manuscript.

Notes

The authors declare no competing financial interest.

■ ACKNOWLEDGMENTS

E.P. and T.A. would like to thank the Leverhulme Trust (RPG2014-225). R.C.S. acknowledges the financial support from ANPCyT (PICT 2016-0679). L.M.A. thanks the KAUST Supercomputing Laboratory using the supercomputer Shaheen II for providing the computational resources.

■ REFERENCES

- (1) Häkkinen, H.; Walter, M.; Grönbeck, H. Divide and Protect: Capping Gold Nanoclusters with Molecular Gold–Thiolate Rings. *J. Phys. Chem. B* **2006**, *110*, 9927–9931.
- (2) Jung, J.; Kang, S.; Han, Y.-K. Ligand Effects on the Stability of Thiol-Stabilized Gold Nanoclusters: Au₂₅(SR)₁₈[−], Au₃₈(SR)₂₄, and Au₁₀₂(SR)₄₄. *Nanoscale* **2012**, *4*, 4206–4210.
- (3) Heaven, M. W.; Dass, A.; White, P. S.; Holt, K. M.; Murray, R. W. Crystal Structure of the Gold Nanoparticle [N(C₈H₁₇)₄]-[Au₂₅(SCH₂CHPh)₁₈]. *J. Am. Chem. Soc.* **2008**, *130*, 3754–3755.
- (4) Qian, H.; Eckenhoff, W. T.; Zhu, Y.; Pintauer, T.; Jin, R. Total Structure Determination of Thiolate-Protected Au₃₈ Nanoparticles. *J. Am. Chem. Soc.* **2010**, *132*, 8280–8281.
- (5) Zeng, C.; Liu, C.; Chen, Y.; Rosi, N. L.; Jin, R. Gold–Thiolate Ring as a Protecting Motif in the Au₂₀(SR)₁₆ Nanocluster and Implications. *J. Am. Chem. Soc.* **2014**, *136*, 11922–11925.
- (6) Tian, S.; Li, Y.-Z.; Li, M.-B.; Yuan, J.; Yang, J.; Wu, Z.; Jin, R. Structural Isomerism in Gold Nanoparticles Revealed by X-Ray Crystallography. *Nat. Commun.* **2015**, *6*, 8667.
- (7) Jadzinsky, P. D.; Calero, G.; Ackerson, C. J.; Bushnell, D. A.; Kornberg, R. D. Structure of a Thiol Monolayer-Protected Gold Nanoparticle at 1.1 Å Resolution. *Science* **2007**, *318*, 430.
- (8) Zhu, M.; Aikens, C. M.; Hollander, F. J.; Schatz, G. C.; Jin, R. Correlating the Crystal Structure of a Thiol-Protected Au₂₅ Cluster and Optical Properties. *J. Am. Chem. Soc.* **2008**, *130*, 5883–5885.
- (9) Zeng, C.; Chen, Y.; Das, A.; Jin, R. Transformation Chemistry of Gold Nanoclusters: From One Stable Size to Another. *J. Phys. Chem. Lett.* **2015**, *6*, 2976–2986.
- (10) Baksi, A.; Chakraborty, P.; Bhat, S.; Natarajan, G.; Pradeep, T. [Au₂₅(SR)₁₈]₂₂[−]: A Noble Metal Cluster Dimer in the Gas Phase. *Chem. Commun.* **2016**, *52*, 8397–8400.
- (11) Krishnadas, K. R.; Baksi, A.; Ghosh, A.; Natarajan, G.; Pradeep, T. Structure-Conserving Spontaneous Transformations between Nanoparticles. *Nat. Commun.* **2016**, *7*, 13447.
- (12) Walter, M.; Akola, J.; Lopez-Acevedo, O.; Jadzinsky, P. D.; Calero, G.; Ackerson, C. J.; Whetten, R. L.; Grönbeck, H.; Häkkinen, H. A Unified View of Ligand-Protected Gold Clusters as Superatom Complexes. *PNAS* **2008**, *105*, 9157.
- (13) Cheng, L.; Yuan, Y.; Zhang, X.; Yang, J. Superatom Networks in Thiolate-Protected Gold Nanoparticles. *Angew. Chem., Int. Ed.* **2013**, *52*, 9035–9039.
- (14) Price, R. C.; Whetten, R. L. All-Aromatic, Nanometer-Scale, Gold-Cluster Thiolate Complexes. *J. Am. Chem. Soc.* **2005**, *127*, 13750–13751.
- (15) Reimers, J. R.; Wang, Y.; Cankurtaran, B. O.; Ford, M. J. Chemical Analysis of the Superatom Model for Sulfur-Stabilized Gold Nanoparticles. *J. Am. Chem. Soc.* **2010**, *132*, 8378–8384.
- (16) Taylor, M. G.; Mpourmpakis, G. Thermodynamic Stability of Ligand-Protected Metal Nanoclusters. *Nat. Commun.* **2017**, *8*, No. 15988.
- (17) Cowan, M. J.; Mpourmpakis, G. Structure–Property Relationships on Thiolate-Protected Gold Nanoclusters. *Nanoscale Adv.* **2019**, *1*, 184–188.
- (18) Li, Z.; Chen, H.-Y. T.; Schouteden, K.; Picot, T.; Liao, T.-W.; Seliverstov, A.; Van Haesendonck, C.; Pacchioni, G.; Janssens, E.; Lievens, P. Unraveling the Atomic Structure, Ripening Behavior, and Electronic Structure of Supported Au₂₀ Clusters. *Sci. Adv.* **2020**, *6*, No. eaay4289.

- (19) Pensa, E.; Albrecht, T. Controlling the Dynamic Instability of Capped Metal Nanoparticles on Metallic Surfaces. *J. Phys. Chem. Lett.* **2018**, *9*, 57–62.
- (20) Kazan, R.; Müller, U.; Bürgi, T. Doping of Thiolate Protected Gold Clusters through Reaction with Metal Surfaces. *Nanoscale* **2019**, *11*, 2938–2945.
- (21) García, C.; et al. Support Effect on the Reactivity and Stability of Au₂₅(SR)₁₈ and Au₁₄₄(SR)₆₀ Nanoclusters in Liquid Phase Cyclohexane Oxidation. *Catal. Today* **2019**, *336*, 174–185.
- (22) Carro, P.; Pensa, E.; Albrecht, T.; Salvarezza, R. C. Dynamics of RS-(Au-SR)_x Staple Motifs on Metal Surfaces: From Nanoclusters to 2D Surfaces. *J. Phys. Chem. C* **2020**, *124*, 5452–5459.
- (23) Qian, H.; Jin, R. Ambient Synthesis of Au₁₄₄(SR)₆₀ Nanoclusters in Methanol. *Chem. Mater.* **2011**, *23*, 2209–2217.
- (24) Parker, J. F.; Weaver, J. E. F.; McCallum, F.; Fields-Zinna, C. A.; Murray, R. W. Synthesis of Monodisperse [Oct₄N⁺][Au₂₅(SR)₁₈⁻] Nanoparticles, with Some Mechanistic Observations. *Langmuir* **2010**, *26*, 13650–13654.
- (25) Horcas, I.; Fernández, R.; Gómez-Rodríguez, J. M.; Colchero, J.; Gómez-Herrero, J.; Baro, A. M. Wsxn: A Software for Scanning Probe Microscopy and a Tool for Nanotechnology. *Rev. Sci. Instrum.* **2007**, *78*, No. 013705.
- (26) Kresse, G.; Joubert, D. From Ultrasoft Pseudopotentials to the Projector Augmented-Wave Method. *Phys. Rev. B* **1999**, *59*, 1758–1775.
- (27) Kresse, G.; Hafner, J. Ab Initio Molecular Dynamics for Liquid Metals. *Phys. Rev. B* **1993**, *47*, 558–561.
- (28) Kresse, G.; Furthmüller, J. Efficiency of Ab-Initio Total Energy Calculations for Metals and Semiconductors Using a Plane-Wave Basis Set. *Comput. Mater. Sci.* **1996**, *6*, 15–50.
- (29) Kresse, G.; Furthmüller, J. Efficient Iterative Schemes for Ab Initio Total-Energy Calculations Using a Plane-Wave Basis Set. *Phys. Rev. B* **1996**, *54*, 11169–11186.
- (30) Blöchl, P. E. Projector Augmented-Wave Method. *Phys. Rev. B* **1994**, *50*, 17953–17979.
- (31) Grimme, S. Semiempirical GGA-Type Density Functional Constructed with a Long-Range Dispersion Correction. *J. Comput. Chem.* **2006**, *27*, 1787–1799.
- (32) Grimme, S.; Antony, J.; Ehrlich, S.; Krieg, H. A Consistent and Accurate Ab Initio Parametrization of Density Functional Dispersion Correction (DFT-D) for the 94 Elements H-Pu. *J. Chem. Phys.* **2010**, *132*, 154104.
- (33) Pearson, W. B., *A Handbook of Lattice Spacings and Structures of Metals and Alloys*; Pergamon Press, 1958, 115.
- (34) Monkhorst, H. J.; Pack, J. D. Special Points for Brillouin-Zone Integrations. *Phys. Rev. B* **1976**, *13*, 5188–5192.
- (35) Noh, J.; Hara, M. Nanoscale Observation of Dissociative Adsorption During Self-Assembly Processes of Dialkyl Disulfides on Au(111). *RIKEN Rev.* **2001**, *37*, 54–57.
- (36) Staub, R.; Toerker, M.; Fritz, T.; Schmitz-Hübsch, T.; Sellam, F.; Leo, K. Flat Lying Pin-Stripe Phase of Decanethiol Self-Assembled Monolayers on Au(111). *Langmuir* **1998**, *14*, 6693–6698.
- (37) Poirier, G. E. Characterization of Organosulfur Molecular Monolayers on Au(111) Using Scanning Tunneling Microscopy. *Chem. Rev.* **1997**, *97*, 1117–1128.
- (38) Lee, S. Y.; Choi, Y.; Ito, E.; Hara, M.; Lee, H.; Noh, J. Growth, Solvent Effects, and Thermal Desorption Behavior of Octylthiocyanate Self-Assembled Monolayers on Au(111). *Phys. Chem. Chem. Phys.* **2013**, *15*, 3609–3617.
- (39) Vericat, C.; Vela, M. E.; Benitez, G.; Carro, P.; Salvarezza, R. C. Self-Assembled Monolayers of Thiols and Dithiols on Gold: New Challenges for a Well-Known System. *Chem. Soc. Rev.* **2010**, *39*, 1805–1834.
- (40) Poirier, G. E.; Tarlov, M. J. The c(4×2) Superlattice of n-Alkanethiol Monolayers Self-Assembled on Au(111). *Langmuir* **1994**, *10*, 2853–2856.
- (41) Poirier, G. E.; Pylant, E. D. The Self-Assembly Mechanism of Alkanethiols on Au(111). *Science* **1996**, *272*, 1145.
- (42) Maksymovych, P.; Sorescu, D. C.; Yates, J. T. Gold-Adatom-Mediated Bonding in Self-Assembled Short-Chain Alkanethiolate Species on the Au(111) Surface. *Phys. Rev. Lett.* **2006**, *97*, 146103.
- (43) Pensa, E.; Azofra, L. M.; Albrecht, T.; Salvarezza, R. C.; Carro, P. Shedding Light on the Interfacial Structure of Low-Coverage Alkanethiol Lattices. *J. Phys. Chem. C* **2020**, *124*, 26748–26758.
- (44) Jabr, N.; Kodlaa, A. DFT Study of Small Gold Clusters Au_n (n=2-13): The Structural, Electronic, Thermodynamic and Spectral Properties. *Chem. Mater. Res.* **2017**, *9*, 17–27.
- (45) Yan, N.; Xia, N.; Liao, L.; Zhu, M.; Jin, F.; Jin, R.; Wu, Z. Unraveling the Long-Pursued Au₁₄₄ Structure by X-Ray Crystallography. *Sci. Adv.* **2018**, *4*, No. eaat7259.
- (46) Lopez-Acevedo, O.; Akola, J.; Whetten, R. L.; Grönbeck, H.; Häkkinen, H. Structure and Bonding in the Ubiquitous Icosahedral Metallic Gold Cluster Au₁₄₄(SR)₆₀. *J. Phys. Chem. C* **2009**, *113*, 5035–5038.
- (47) Dee, K. C.; Puleo, D. A.; Bizios, R., Protein-Surface Interactions. In *An Introduction to Tissue-Biomaterial Interactions*, 1st ed.; John Wiley & Sons, Inc: Hoboken, New Jersey, 2002; 37–52.
- (48) Guedes-Sobrinho, D.; Wang, W.; Hamilton, I. P.; Da Silva, J. L. F.; Ghiringhelli, L. M. (Meta-)Stability and Core-Shell Dynamics of Gold Nanoclusters at Finite Temperature. *J. Phys. Chem. Lett.* **2019**, *10*, 685–692.
- (49) Malola, S.; Häkkinen, H. Chiral Inversion of Thiolate-Protected Gold Nanoclusters Via Core Reconstruction without Breaking a Au–S Bond. *J. Am. Chem. Soc.* **2019**, *141*, 6006–6012.
- (50) Ouyang, R.; Jiang, D.-E. Ligand-Conformation Energy Landscape of Thiolate-Protected Gold Nanoclusters. *J. Phys. Chem. C* **2015**, *119*, 21555–21560.
- (51) Huang, Y.; Liu, W.; Cheng, H.; Yao, T.; Yang, L.; Bao, J.; Huang, T.; Sun, Z.; Jiang, Y.; Wei, S. Solvent-Induced Desorption of Alkanethiol Ligands from Au Nanoparticles. *Phys. Chem. Chem. Phys.* **2016**, *18*, 15927–15933.
- (52) Holmes, S.; Gao, J.; Tang, L.; Li, F.; Palmer, R. E.; Guo, Q. Bridge-Bonded Methylthiolate on Au(111) Observed with the Scanning Tunneling Microscope. *Phys. Chem. Chem. Phys.* **2018**, *20*, 19486–19491.
- (53) Gao, J.; Li, F.; Zhu, G.; Yang, Z.; Lu, H.; Lin, H.; Li, Q.; Li, Y.; Pan, M.; Guo, Q. Spontaneous Breaking and Remaking of the RS–Au–SR Staple in Self-Assembled Ethylthiolate/Au(111) Interface. *J. Phys. Chem. C* **2018**, *122*, 19473–19480.